29th Congress of the International Council
of the Aeronautical Sciences
St. Petersburg, Russia; September 7–12, 2014

CHARACTERISING INTERNAL HEAT TRANSFER IN THERMAL PROTECTION SYSTEMS

N. Banerji* , P. Leyland* , S. Haussener**
Ecole Polytechnique Fédérale de Lausanne
*Interdisciplinary Aerodynamics Group (IAG)
**Laboratory of Renewable Energy Science and Engineering (LRESE)

Keywords: *atmospheric re-entry, aerodynamic heating, porous media, tomography, monte carlo*

Abstract

Thermal protection systems (TPS) are employed for spacecraft to survive high temperature conditions during atmospheric re-entry. For space shuttle type re-entries, the use of ceramic tiles shield the payload from exposure to these high heat fluxes. Recent research into the use of low-density materials, such as alumina foams, brings its own scientific challenges, of which understanding internal heat transfer is one. To this end, the exact 3D geometry of their complex porous structures, before and after plasma torch heating, is obtained by tomography and used in direct pore-level simulations to numerically calculate their effective heat transfer properties. Morphological characterisation is conducted via two-point correlation functions and mathematical morphology operations. Porosity and hydraulic pore diameter are seen to increase from the pre-heating (virgin) to the post-heating (charred) sample. Collision-based Monte Carlo methods are then used for radiative heat transfer characterisation. A decrease in extinction coefficient is noted between the virgin and charred samples. Both samples exhibit a large backward scattering peak for diffusely reflecting surfaces.

1 General Introduction

Aerodynamic heating during hypersonic atmospheric re-entry is a chief constraint for spacecraft design and relates to the hot gas in the flowfield surrounding the vehicle. The high temperature in the boundary layer adjacent to the vehicle surface is due to internal viscous effects slowing the entering high kinetic energy hypersonic flow, dissipating and transforming it into internal energy of the gas [1].

In the case of low Earth orbit (LEO) re-entries, heat is transferred to the vehicle predominantly via thermal conduction (dependent on the temperature gradient in the gas at the wall and often called convective heating) and to a lesser extent, radiation. To survive and ensure the safety of the payload, LEO re-entry vehicles are equipped with re-usable Thermal Protection Systems (TPS) which insulate the exterior using a material with near-zero thermal conductivity. In general, re-usable materials such as reinforced carbon-carbon (RCC) are used for the most heat exposed components of the TPS. They consist of a carbon-carbon composite with a triple pre-pyrolysed resin and a silicon carbide (SiC) coating to prevent oxidation during re-entry [2].

More than fifty years since man first exited the Earth's atmosphere and was brought back safely, TPS sizing still involves significant uncertainties. Large margins are therefore applied to its design, which increase structural and fuel weight and decrease useable payload size. Optimising TPS design is thus imperative. State of the art research studies, amongst other options, low-density TPS materials which bring new scientific challenges - of which internal heat

transfer is concentrated on in this paper.

Due to the economic infeasibility of flight testing, re-entry conditions are recreated on the ground using experimental facilities. Plasma torch facilities can be used to heat the TPS materials to the extreme temperatures expected during re-entry [3]. This paper will report progress of the study of internal heat transfer processes in a candidate TPS material under re-entry conditions recreated by plasma torch experiments. Computer tomography (CT) enables the digitisation of exact geometries of the complex porous structures, of the virgin and charred sample, required for the direct pore level numerical simulations. Previous pertinent studies include the determination of the extinction and scattering coefficients as well as the scattering phase function of metal foams and reticulate porous ceramics (RPCs) using CT based methods [4, 5].

2   Materials

Alumina foam has been proposed as a TPS candidate material [6] and possible replacement for RCC's due to its very low density, thermal conductivity and high melting temperature.

2.1   Sample Preparation

A high purity alumina ceramic (Al_2O_3) with tailorable porosity and easy machinability was used. The samples were prepared from high purity alpha alumina particles (CT3000SG [7]), the nominal composition of whom is listed in table 1. The median particle diameter d_{50} is 0.5 μm and the average specific surface area 7.2 m^2/g.

The foam was prepared by De Cavis Technology, Zürich. Their methodology is based on stabilising a foam of a solution containing alumina particles. First, they are partially hydrophobised by adsorbing carboxylic acids to the particle surface [8]. A solution containing these particles is then mechanically foamed and

Component	Content (% weight)
Na_2O	0.08
MgO	0.07
SiO_2	0.03
CaO	0.02
Fe_2O_3	0.02
Al_2O_3	> 99

Table 1 Nominal composition of alumina particles used for alumina foam production [7].

dried once stable. This results in a green body stable foam, which is then sintered at 1850°C to produce the final closed-pore ceramic foam. Finally the ceramic foams are machined to the final dimensions using a diamond edged saw. The manufacturer characterised the foam's geometric properties, shown in table 2.

Porosity	89.5%
Density	0.42 g/cm^3
Mean pore diameter	400 μm

Table 2 Geometric characterisation of alumina foam samples [6].

2.2   Plasma Torch Experimental Campaign

The plasma torch campaign for alumina foam was conducted [9] in 2011 with the aim of measuring the ultra violet (UV) emission spectra. The test conditions and set-up are summarised in table 3. An alumina foam sample was exposed to a plasma torch, varying parameters such as material-torch distance and test duration. The chamber pressure was maintained at 0.3 mbar. The plasma is created by Tungsten electrodes passing a current of 600 A through a test gas composed of 90% Ar and 10% N_2. The plasma temperature was estimated in the region of 3500-4000 K. Although it is noted that during shuttle re-entry, ceramic tile temperatures did not much exceed 1200 K [10], a worst case scenario could be envisaged here.

During the first shot, metal holders of the sample melted before the end of the experiment. A thin char layer formed on the sample surface,

Shot no.	Distance (m)	Duration (min)
1	1.0	2.5
2	1.0	5.0
3	0.7	3.5
4	0.4	3.0

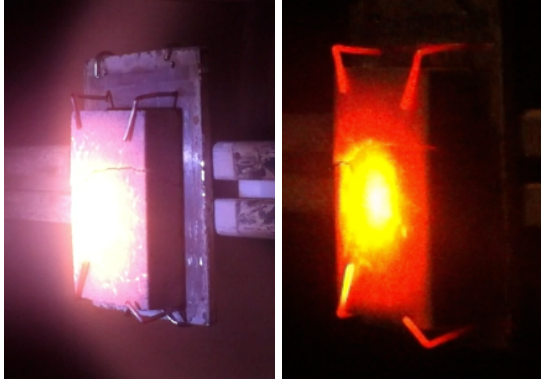**Table 3** Summary of test conditions [6].

Fig. 1 The sample (a) during and (b) right after shot 1 [9].

prevalent near the metal holders due to the added conduction effects. The holders were changed to tungsten hooks (figure 1), more resistant to high temperatures, and thus were used for subsequent shots. As the torch was made to approach the foam sample, heat penetrated deeper into the porous structure. This created small fissures which grew larger until catastrophic failure of the material. With each shot the surface charring increased.

2.3 Sample Characterisation

Leyvraz [6] conducted X-ray photoelectron spectroscopy (XPS), scanning electron microscopy (SEM) and energy dispersive X-ray spectroscopy (EDX) characterisation of the virgin and charred samples.

An Axis Ultra XPS machine was used in vacuum with a monochromatic Al Kα source at 1486.6 eV to produce the X-rays, working at 150 W. Table 4 presents the species concentrations at the surface of both virgin and charred samples. It is clear that the chemical composition differs

from the nominal composition. Carbon appears to be deposited on both surfaces, as well as the introduction of sodium content. This can be explained by the unsealed storage of samples for over a year between plasma torch testing and characterisation, as ageing causes the carbon deposition. However, the increased carbonisation of the charred sample is also evident, as is to be expected. The increase of sodium content is mostly likely also the product of contamination via handling, no sodium was present in the plasma.

Species	Concentration (% weight)		
	Nominal	Virgin	Charred
O	> 59.5	37.1	15.0
Al	> 39.6	11.9	1.5
C	0	40.4	79.6
N	0	6.3	0.0
Na	0.03	4.2	4.0

Table 4 Quantitative XPS analysis [6].

The samples were also characterised with a MERLIN (Zeiss, Germany) scanning electron microscope, equipped with EDX capabilities. Figure 2 shows SEM images of the virgin and charred samples with 154x magnification. Increasing magnification to 9850x reveals nano-flaking at the charred zones, as shown in figure 3. EDX analysis of the alumina and carbon nano-flake zones reasserted the presence of additional carbon content in specifically charred locations [6].
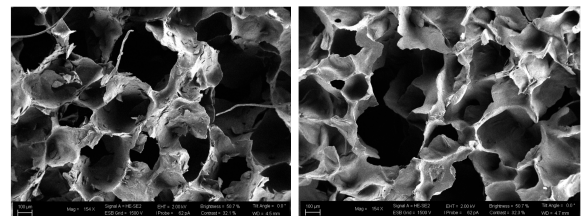

Fig. 2 SEM images of (a) virgin and (b) charred samples with 154x magnification [6].

The plasma chamber seems to not have been properly cleaned before testing, with soot

coating the inner walls and the sample holder. This carbon residue could have contaminated the argon and nitrogen gas. Nevertheless, there was a carbon phase in the virgin sample that nucleated and grew with exposure to plasma.
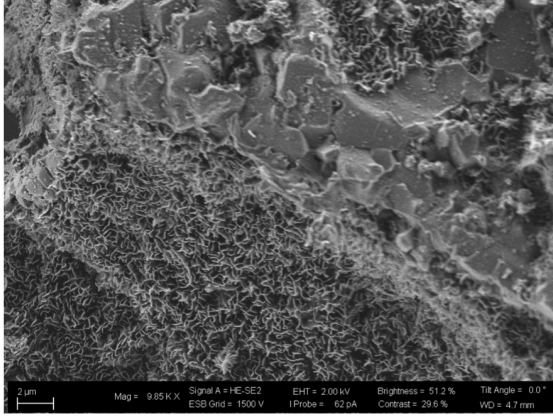

Fig. 3 SEM image of the transition zone between alumina and nano-flake structure [6].

With regards to the relative lack of change in pore-scale morphology (figure 2), even if there was melting on the surface, it was probably only a thin layer at a time, which, once liquid, was most likely blown away by the plasma. Due to the ambiguous recording of test conditions, it is difficult to judge the occurrence of any ablation. On a microscopic scale, however, a change in morphology is observed (figure 3) as the alumina at the sample surface no longer shows any grains, indicating sintering or even local fusion. This is an expected result as the plasma temperature largely exceeded the melting point of alumina. This change is seen and quantified in the numerical morphological characterisation presented in the section below.

3 Morphological Characterisation

3.1 Low-resolution CT

The nominal pore diameter of the virgin sample is $d_{nom} = 400$ μm [6], corresponding to 63.5 pores per inch (ppi). The sample is exposed to an unfiltered polychromatic X-ray beam produced by a Viscom XT-9160-TXD X-ray tube. The low-resolution computed tomography (LRCT) parameters are presented in table 5 for both virgin and charred samples. A Perkin Elmer XRD 1621 CN3 ES CT-Grade detector, without filters, is used to detect the transmitted X-rays. Each projection consists of an average over four scans, with an exposure time per scan of 0.7 s for full field of view (FFOV) and 0.1 s for zoom.

	Virgin		Charred	
	Zoom	FFOV	Zoom	FFOV
V (kV)	60	80	60	80
I (μA)	160	125	160	125
Proj. angles	720	720	720	1080
Exp. time	4s	2.8s	4s	2.8s
Vox. size	2.99 μm	20 μm	2.99 μm	2.99 μm
FoV (mm)	$3.58 \times 3.58 \times 2.99$	$24 \times 24 \times 40$	$3.88 \times 3.88 \times 2.99$	$29 \times 29 \times 28$

Table 5 LRCT parameters.

The CT data consists of 2 byte (0-65535) optical density values $\alpha(x)$ arranged on a 3D cartesian grid. In order to digitalise the data for use in morphological and heat transfer characterisation, the phases must first be identified, assigning each voxel to one phase via the process of segmentation. Unfortunately the tomographic data obtained has a low signal to noise ratio, making manual segmentation a challenging task as the image histograms often contain only a single discernible peak.

To improve chances of success in segmentation, pre-processing is conducted using the ImageJ software suite [11]. The adopted approach for the virgin sample tomography data involves converting to 8 bit data and varying brightness to be able to distinguish the solid structure from the void. A median filter is then used, which blurs the image by replacing each pixel with the median of its 3×3 neighbourhood. The `Try All` feature of the automatic thresholding tool is then employed. This produces a montage with results from all the inbuilt thresholding methods [12], allowing the user to compare, side by side, how the different algorithms perform on a particular image. From this, the most appropriate algorithm is chosen by eye, using the

preservation of struts (i.e. lack of black spots in the struts) as well as the absence of spots across the image stack and good contrast as selection criteria.

For the best possible dataset, of all tomographic slices obtained for each sample, the first and last hundred were discarded. A similar methodology is used for the charred samples, with the added use of the inbuilt smoothing function instead of use of the median filter. This filter blurs the image by replacing each pixel with an average of its 3×3 neighbourhood. The smoothing function seemed to facilitate the subsequent thresholding process, removing most spots from struts. This segmentation threshold is then used to convert the grey level matrix into a $0/1$ matrix where a value of one means the point lies within the void and zero that it lies within the solid phase.

3D surface renderings of sample sub-volumes, reconstructed from the resulting tomography data, are shown in figure 4 for both samples. Since the focus is on a two-phase system, evaluation of porosity, specific surface area and representative elementary volume (REV) is important.
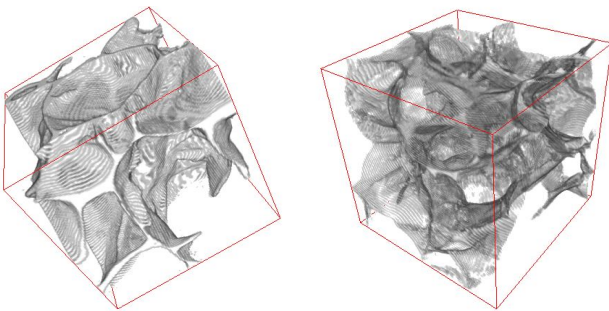

Fig. 4 3D surface rendering of 2.99 μm voxel size tomography data for (a) virgin and (b) charred samples.

3.2 Porosity and Specific Surface Area

The porosity and specific surface area are calculated via a two-point correlation function using Monte Carlo sampling (figure 5), the

equations for which are described in detail by Haussener [4]. For this, a random point is chosen within the void phase and a second point is chosen at distance r. If the second point belongs to the same phase, the integrand is equal to one, otherwise it is equal to zero. The computation is performed for 10^8 random points, for 0 cm $\leq r \leq 1$ cm. The results of these calculations are given in table 6.
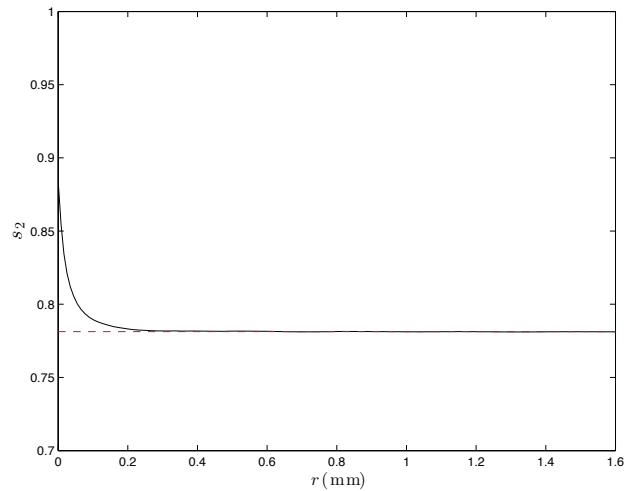

Fig. 5 Two point correlation function for the virgin sample with voxel size 2.99 μm. The value at $r = 0$ is the calculated porosity and the dashed line indicates the asymptotic value of the function corresponding to ε^2.

	Vox. size	ε	SSA (m^{-1})
Virgin	2.99 μm	0.8839	14345
	20 μm	0.9295	3978
Charred	2.99 μm	0.9481	8387
	20 μm	0.9337	3632

Table 6 Porosity and specific surface area (SSA).

It can be seen that both porosity and specific surface area depend on the voxel size of the scan. The porosity for the virgin sample is calculated at $\varepsilon = 0.88$ and $\varepsilon = 0.93$ for voxel sizes of 2.99 μm and 20 μm respectively. This compares favourably with the manufacturer supplied value of $\varepsilon = 0.895$, giving an error of 1.67% and 3.9% for the zoom and full field of view data respectively. The porosity of the charred sample

is calculated higher at $\varepsilon = 0.95$ and $\varepsilon = 0.93$ for zoom and FFOV data respectively. This compares well with the changes between virgin and charred samples, visualised qualitatively by Leyvraz on the microscopic scale during sample characterisation.

The specific surface area A_0 is expected to be inversely proportional to voxel size due to better resolution of surface irregularities, as is the case for both samples. For a voxel size of 2.99 μm, the specific surface area decreases significantly from 14345 m^{-1} for the virgin sample to 8387 m^{-1} for the charred sample. This could be an after effect of the usage of the smoothing function during pre-processing which may reduce surface irregularities. This hypothesis would need to be further explored by avoiding use of smoothing during pre-processing for the charred sample, but is left out of this paper due to time constraints.

3.3 REV

The representative elementary volume (REV) is defined as the smallest volume of a porous material which can be considered as continuum, i.e. that results in statistical meaningful local average properties. It is determined based on porosity calculations for subsequently increasing volumes at 20 random locations in the sample (figure 6), until it asymptotically reaches a constant value within a band of $\pm\gamma$. For an edge length l approaching 0, the porosity is either 0 or 1, depending on whether it is in the void or solid phase. Haussener [4] details equations required to calculate the edge length $l_{\mathrm{REV},\gamma}$ of the cubic REV.

For $\gamma = 0.05$, for the virgin sample $l_{\mathrm{REV},\gamma} = 0.79$ mm and 2.339 mm for the scans with voxel sizes 2.99 μm and 20 μm corresponding to $1.98d_{\mathrm{nom}}$ and $5.85d_{\mathrm{nom}}$ respectively. For the charred sample, $l_{\mathrm{REV},\gamma} = 0.60$ mm and 1.605 mm for the scans with voxel sizes 2.99 μm and 20 μm corresponding to $1.56d_{\mathrm{nom}}$ and $4.01d_{\mathrm{nom}}$ respectively.
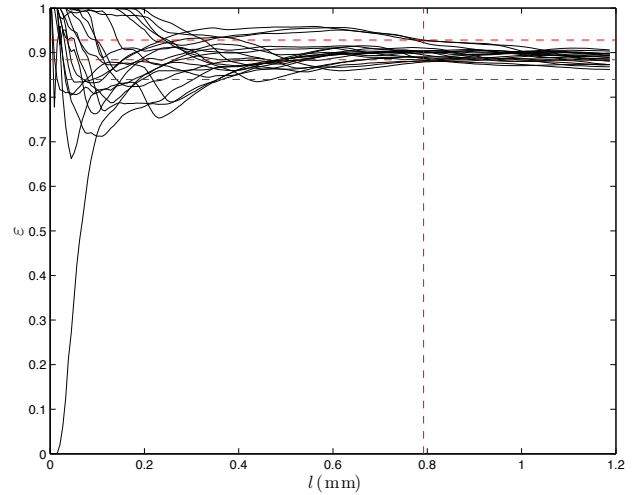

Fig. 6 Determination of the REV edge length (indicated by the vertical dashed line) for the virgin sample with voxel size 2.99 μm. The tolerance band for conversion and determination of the REV volume at $\varepsilon \pm \gamma$.

3.4 Sensitivity to Segmentation Threshold

During morphological characterisation, it was seen that the segmentation threshold played an extremely important role in the variation of results. This is most likely due to the poor quality of tomographic data which leads the image histograms to have only one discernible peak (seen in figure 7), leading to any significant variations in threshold value incorrectly segmenting the data or even missing the peak entirely. When this information would then come to be digitised, the void phase could be assumed part of the solid phase or vice versa. As seen in the image, there is more room for error in this with reference to the zoom data as compared to the FFOV as the zoom has a wider distribution and a small second peak can be seen.

This sensitivity is demonstrated in the figure 8 for data of voxel size 2.99 μm and 20 μm for both virgin and charred samples. For a 5% variation in segmentation threshold, the digitising process is greatly affected leading to errors which are carried over to the morphological characterisation operations. Numerically calculated porosity for the virgin zoom sample can vary between -3% and 1.5%. For the
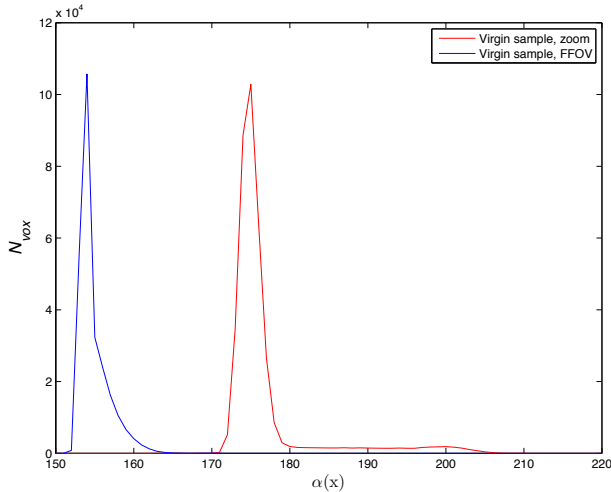
Fig. 7 Histograms of absorption values for scans of the virgin sample with voxel size 2.99 μm (zoom) and 20 μm (FFOV).

specific surface area, this variation is higher, between 28.5% and -1.3%. The same can be seen of REV edge length, where this variation is between 3.3% and 9.1%. The char zoom data has slightly larger variations as the tomography scans were of worse quality.
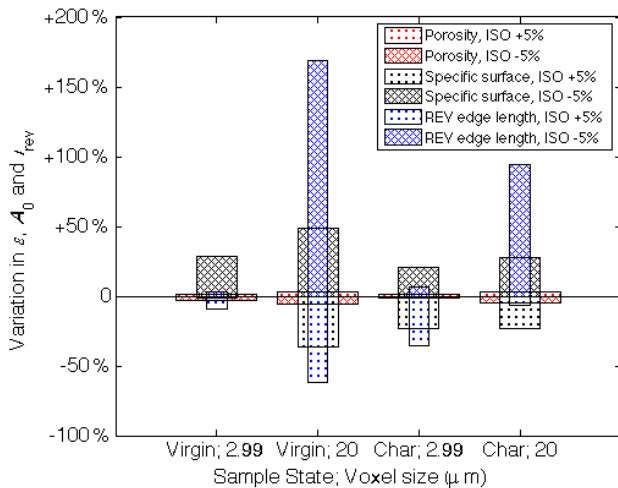

Fig. 8 Variation of porosity, specific surface area and REV edge length with a $\pm$5% variation in segmentation threshold.

For the aforementioned reasons, 20 μm voxel size data is clearly the more sensitive of the two sets, and therefore is best not used for radiative characterisation calculations. This

suggests the need for better quality tomographic data and better segmentation algorithms. It is also suggested that this sensitivity analysis is conducted using absolute rather than relative changes to the threshold values, to be able to better compare the 2.99 μm and 20 μm voxel size data. A two-point correlation is still the best to determine morphological characteristics [5], but good results can only be achieved if the underlying digitised morphology resembles reality.

4 Radiative Characterisation

Methodology to determine effective radiative properties of two-phase media is defined in detail by Haussener [5]. Collision-based Monte Carlo methods are applied with geometric optics assumed. This assumption is true when the characteristic size parameters $\pi d_h/\lambda >> 1$ for both phases. Due to the expected material temperatures during re-entry conditions, radiative characterisation of the samples is conducted for the near infrared (IR) range, between the wavelengths of $1000 - 2000$ nm. Therefore in the cases studied, the assumption for geometric optics is valid. The fluid phase is assumed to be radiatively nonparticipating. A diffusely reflecting solid-fluid interface was implemented, with $\rho = 0.87$.

A sub volume of $600 \times 600 \times 600$ pixels was used for the Monte Carlo calculations, for a voxel size of 2.99 μm corresponding to a sample size of $1.8 \times 1.8 \times 1.8$ mm. This sample is larger than the minimum REV edge length requirement, but it was thought prudent to use as large a volume as possible to calculate the continuum scale effective radiative characteristics. The full field of view dataset was also investigated, for purposes of comparison between the two resolutions. For a voxel size of 20 μm, a sub volume of $500 \times 500 \times 500$ pixels corresponding to a sample size of $10 \times 10 \times 10$ mm was studied.

	Vox. size (μm)	β (m^{-1})	$\sigma_{1,1}$ (m^{-1})
Virgin	2.99	3680	3115
	20	1035	901
Charred	2.99	3380	2940
	20	1368	1190

Table 7 Evaluation of extinction and scattering coefficients for virgin and charred samples, for a voxel size of 2.99 μm and 20 μm.

A least-square fit to Bouguer's law yields an extinction coefficient (table 7) of $\beta_{\text{virgin}} = 3680$ m^{-1} for the virgin sample, with RMS $= 0.01$. For the charred case, the extinction coefficient is calculated to be $\beta_{\text{char}} = 3380$ m^{-1}. Both values are constant over the studied wavelength range. The extinction coefficient of the charred sample is thus lower than that of the virgin sample. By rule of thumb, β is expected to be inversely proportional to pore size. The hydraulic pore diameter ($d_{\text{h,pore}} = \frac{4\varepsilon}{A_0}$) for the virgin sample is $d_{\text{h,pore}} = 0.246$ mm and for the charred sample is $d_{\text{h,pore}} = 0.452$ mm, thus demonstrating this expected outcome.

The scattering coefficients (table 7) are a function of the surface reflectivity and calculated to be $\sigma_{1,1} = 3115$ m^{-1} for the virgin sample decreasing to $\sigma_{1,1} = 2940$ m^{-1} for the charred sample. This is expected since the scattering albedo ($\omega = \frac{\sigma}{\beta}$) should be similar for the virgin and charred samples and equal to the diffuse reflectivity, ρ. Thus a decrease in extinction coefficient, as is the case from virgin to char, leads to a decrease in scattering coefficient.

For the diffusely reflecting surface of the solid phase, the scattering phase function is plotted as the cosine of the scattering angle, as shown in figure 9. It is well approximated (RMS$= 0.012$) for the virgin sample,

$$\Phi = 0.4390\mu_s^2 - 1.2840\mu_s + 0.8230 \quad (1)$$

For the charred sample, with RMS $= 0.010$,

$$\Phi = 0.3571\mu_s^2 - 1.2614\mu_s + 0.8788 \quad (2)$$

The virgin sample and charred sample both

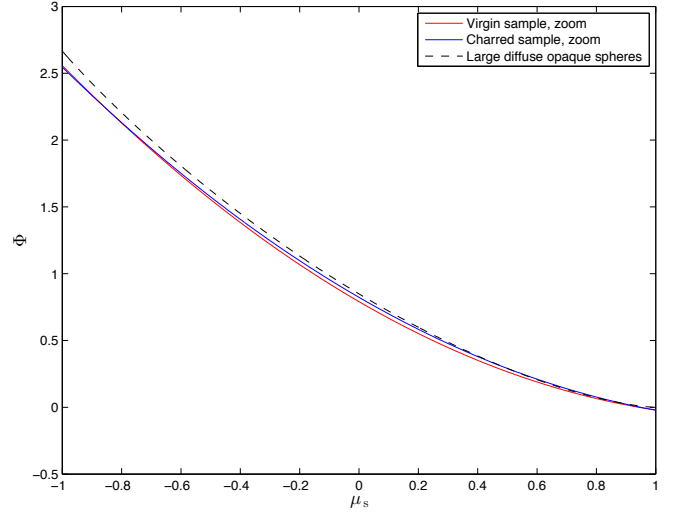**Fig. 9** Scattering phase functions of the virgin and charred samples (voxel size 2.99 μm) compared to analytically calculated function for large diffuse opaque spheres as a function of the cosine of scattering angle.

exhibit a large backward scattering peak for diffusely reflecting surfaces. An analytically determined scattering phase function for diffusely-reflecting large opaque spheres [13] has also been plotted in figure 9. This analytical function is presented in equation 3 and demonstrates good correlation with the virgin and charred samples, showing predominant backward sampling.

$$\Phi(\Theta) = \frac{8}{3\pi}(\sin\Theta - \Theta\cos\Theta) \quad (3)$$

It is often simpler to describe directional scattering behaviour by the so called asymmetry factor, g, which is the average cosine of the scattering angle. It is related to the phase function by equation 4. For isotropic scattering, $g = 0$, for predominant forward scattering, $g > 0$ and for predominantly backward scattering $g < 0$ [13].

$$g = \overline{\cos\Theta} = \frac{1}{4\pi}\int_{4\pi}\Phi(\Theta)\cos\Theta\,d\Omega \quad (4)$$

For the virgin sample, it is calculated that $g_{\text{zoom}} = -0.4297$ and $g_{\text{FFOV}} = -0.4280$, which indicates that radiation is mostly backward scattered. For the charred sample, $g_{\text{zoom}} = -0.4511$ and $g_{\text{FFOV}} = -0.4146$, thus also indicating predominantly backward scattering.

4.1 Sensitivity to Segmentation Threshold

The data presented in figures 10 and 11 is for both char and virgin samples for a voxel size of 2.99 μm and 20 μm. For a 5% variation in segmentation threshold, extinction coefficient varies between 6.2% and -1.46% and scattering coefficient varies identically as expected for the virgin sample of voxel size 2.99 μm. For the same resolution, the results for the char sample demonstrate higher sensitivity to segmentation threshold variations, which is expected due to the quality of tomographic data. Asymmetry factor is a lot less sensitive to segmentation threshold than the above values, with only a 5.8% variation for the virgin sample and a 3.5% variation for the charred sample at 2.99 μm.
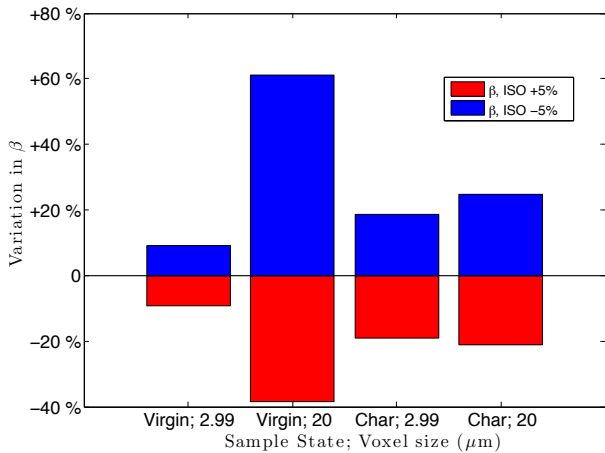

Fig. 10 Variation of extinction coefficients with a $\pm$5% variation in segmentation threshold.
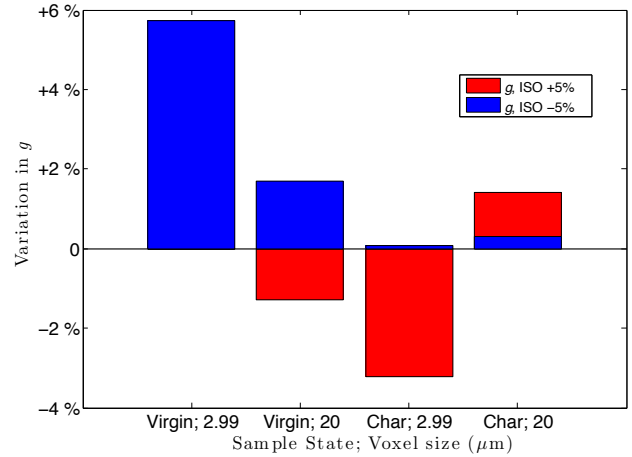

Fig. 11 Variation of asymmetry factor, g with a $\pm$5% variation in segmentation threshold.

5 Conclusions and Future Work

A sample of alumina foam with porosity $\varepsilon = 0.895$ was heated to between 3500 - 4000K using a plasma torch facility. The exact 3D morphology of its complex porous structure was then recorded using low resolution computed tomography for voxel sizes of 2.99 μm and 20 μm, and digitised after pre-processing using ImageJ. Porosity, specific surface area and REV edge length were then successfully characterised using direct pore level simulations for both samples at both resolutions.

In the case of the higher resolution data, an increase in porosity was calculated, from $\varepsilon = 0.88$ before heating to $\varepsilon = 0.95$ post heating. The hydraulic pore diameter of the charred sample is $d_{\text{h,pore}} = 0.452$ mm compared to $d_{\text{h,pore}} = 0.246$ mm for the virgin sample. The specific surface areas were calculated at 14345 m^{-1} and 8387 m^{-1} for the virgin and charred samples respectively. This drastic change in value is thought to be the result of the pre-processing conducted on the charred data (via use of a mean filter), as well as sensitivity to segmentation threshold, detailed further below. The REV determined was 0.49 mm^3 for the virgin and 0.216 mm^3 for the charred sample. However, the sample size used for radiative characterisation was 5.77 mm^3 in both cases,

to allow for a larger data sample and more generalised continuum scale results for the materials.

For the full field of view data (voxel size 20 μm), an increase in porosity was again seen, from $\varepsilon = 0.929$ before heating to $\varepsilon = 0.934$ post heating. The hydraulic pore diameter of the charred sample is $d_{h,pore} = 1.03$ mm compared to $d_{h,pore} = 0.935$ mm for the virgin sample. The specific surface areas were calculated at 3978 m^{-1} and 3632 m^{-1} for the virgin and char samples respectively. The REV determined was 12.8 mm^3 for the virgin sample and 4.13 mm^3 for the charred sample. Extreme sensitivity to threshold segmentation values as well as poor correlation with the morphological results for the low resolution data meant that radiative characterisation carried out for this data was untrustworthy and discounted. These results are therefore not presented in the conclusions.

Collision-based Monte Carlo methods were used for radiative heat transfer characterisation, assuming geometric optics, on the higher resolution data of voxel size 2.99 μm. A decrease in extinction coefficient is noticed between virgin ($\beta_{virgin} = 3680$m^{-1}) and charred ($\beta_{char} = 3380$m^{-1}) samples. This is expected, as extinction coefficient is inversely proportional to pore size, which increases for the charred sample. Using the computed asymmetry factor, g, it is also noted that the charred sample ($g = -0.4297$) and the virgin sample ($g = -0.4511$) exhibit a large backward scattering peak for diffusely-reflecting surfaces. The scattering coefficients were a function of the surface reflectivity and determined to be $\sigma_{1,1} = 3115$ m^{-1} for the virgin sample decreasing to $\sigma_{1,1} = 2940$ m^{-1} for the charred sample. This is expected since the scattering albedo ($\omega = \frac{\sigma}{\beta}$) should be similar for the virgin and charred samples and is the same as the diffuse reflectivity (ρ). Thus a decrease in extinction coefficient, as is the case from virgin to char, leads to a decrease in scattering coefficient.

The quality of the tomographic data and thresholding algorithms must be improved. As previously mentioned, the histograms for absorption values of the scans do not have a wide enough distribution and are often confined to having a single peak. Therefore a small change in segmentation threshold can cause the data to be poorly segmented during digitisation, vastly affecting the results of the numerical calculations that follow. However, successful morphological and radiative characterisation was achieved and experimental comparison of these results would be an interesting future study. It is also recommended to redo the plasma torch experiments under more controlled conditions to reproduce the realistic effects of aerodynamic heating of TPS materials during re-entry.

The results of this study further the understanding of the internal radiative heat transfer in a low density alumina foam destined for TPS usage.

References

[1] John David Anderson. *Hypersonic and high temperature gas dynamics.* Aiaa, 2000.

[2] Karen H Lyle and Edwin L Fasanella. Permanent set of the space shuttle thermal protection system reinforced carbon–carbon material. *Composites Part A: Applied Science and Manufacturing*, 40(6):702–708, 2009.

[3] Monika Auweter-Kurtz, Helmut L Kurtz, and Stefan Laure. Plasma generators for re-entry simulation. *Journal of Propulsion and Power*, 12(6):1053–1061, 1996.

[4] Sophia Haussener, Patrick Coray, Wojciech Lipinski, Peter Wyss, and Aldo Steinfeld. Tomography-based heat and mass transfer characterization of reticulate porous ceramics for high-temperature processing. *Journal of Heat Transfer*, 132(2):023305, 2010.

[5] S. Haussener. *Tomography based determination of effective heat and mass transport properties of complex multi-phase media*. PhD thesis, ETH Zürich, 2010.

[6] David Leyvraz. Thermal protection systems materials for space applications. Technical

report, Ecole Polytechnique Federale de Lausanne, Lausanne, 2012.

[7] Almatis. Reactive Alumina CT 3000 LS SG - safety data sheet.

[8] Urs T. Gonzenbach, André R. Studart, David Steinlin, Elena Tervoort, and Ludwig J. Gauckler. Processing of particle-stabilized wet foams into porous ceramics. *Journal of the American Ceramic Society*, 90(11):3407–3414, November 2007.

[9] Ojas Joshi, Sami Goecke, and David Grange. Ceramic foam samples tested in plasma torch facility. Technical report, Ecole Polytechnique Federale de Lausanne, Lausanne, 2011.

[10] Kenneth W Iliff and Mary F Shafer. Space shuttle hypersonic aerodynamic and aerothermodynamic flight research and the comparison to ground test results. 1993.

[11] Caroline A Schneider, Wayne S Rasband, Kevin W Eliceiri, Johannes Schindelin, Ignacio Arganda-Carreras, Erwin Frise, Verena Kaynig, Mark Longair, Tobias Pietzsch, Stephan Preibisch, et al. Nih image to imagej: 25 years of image analysis. *Nature methods*, 9(7), 2012.

[12] Prasanna K Sahoo, SAKC Soltani, and Andrew KC Wong. A survey of thresholding techniques. *Computer vision, graphics, and image processing*, 41(2):233–260, 1988.

[13] Michael F Modest. *Radiative heat transfer.* Academic Press, 2013.

6   Acknowledgements

7   Contact Author

mailto: nikhil.banerji@epfl.ch
mailto: penelope.leyland@epfl.ch
mailto: sophia.haussener@epfl.ch

Copyright Statement